Digital Peak Current Program Mode Controller for Switched Reluctance Machines

Rajdeep Banerjee, *Student Member, IEEE*, and Parthasarathi Sensarma, *Senior Member, IEEE*

***Abstract*—This article proposes a digital peak current program mode control scheme for switched reluctance machine (SRM) drives. To control phase currents, in general, a hysteresis controller (HC) is widely used due to its simplicity and robustness. However, realizing HC on a digital platform requires a significantly high ratio of sampling to switching frequency. To obviate such steep demands on data sampling, the proposed scheme uses the precepts of the digital current program mode control, widely used for dc–dc converters. For amenability with the SRM drive, this article proposes a transformation that represents an SRM by its dc-equivalent circuit. This transformation also simplifies the mathematical modeling of the drive. Then, to consider variations in phase-inductance and back-emf, parameter adaption through real-time estimations is incorporated in the proposed scheme. A stability criterion is derived from the robustness analysis by probing the effect of estimation errors on reference tracking performance. Finally, the proposed scheme is experimentally validated using a 1 kW, 3000 r/min 6/4 SRM-based laboratory prototype. Also, the proposed scheme is bench-marked against the conventional HC and model predictive control scheme, realized on the same digital platform.**

***Index Terms*—Current control, digital controller, switched reluctance machine.**

I. Introduction

SWITCHED reluctance machines (SRM) are suitable for modern applications, such as electric-vehicle, air-craft propulsion, and pumps [1], [2], [3], [4], due to their inverse torque speed characteristics and inherent fault-tolerant capability. For SRM drives, a two-loop hierarchical control structure, comprising inner-current and outer speed control-loops, is widely considered. However, the current controller design is complicated by the plant nonlinearity, as the phase inductance varies with rotor position (θ) and excitation current (i), and the back-emf with both rotor speed (ω) and i. Also the developed shaft torque is proportional to i^2. As reported in [6], [7], [8], [9], [10], [11], and [12], PI-based and hysteresis control (HC) are two distinct and popular approaches for current regulation in SRM drives.

One of the major advantages of a PI-based controller is the fixed switching frequency. However, its design entirely depends on the equilibrium conditions considered to derive the plant transfer function for the inner current control loop. In [6], to eliminate the nonlinearity due to back-emf, the plant transfer function is derived considering constant ω. Also, this nonlinearity can be eliminated using back-emf compensation [5], [6], [7], [8], [9], [10]. In [5], back-emf is estimated using the sensed i and ω. However, the variation in phase inductance (L) is neglected. This leads to improper design and eventually causes poor reference tracking and oscillations [7], [8]. Therefore, in [7], the phase-inductance adaptive control law was proposed, with the proportional coefficient made a function of the incremental inductance. However, in [8], both proportional and integral coefficients are defined as functions of θ and i, which accounts for the variation of L indirectly. Then, to decouple the back-emf component, 2-D look-up table (LUT) is used to store it as a function of i and θ. Use of LUT is avoided in [10] through a linearized analytical model for the back-emf.

Unlike PI-based methods, plant model of the current control loop minimally influences design of a HC [11], [12]. Also, high control bandwidth and robustness against parameter variation are some of its major advantages. Though the fixed hysteresis error-band defines the allowable current-ripple, it causes variable switching frequency f_{sw} due to variation in L. This increases the machine vibration and acoustic noise. Therefore, in [13], the error band is varied with L to achieve constant f_{sw}. However, the need for continuous error comparison makes the realization of HC, on a digital platform, demand a high sampling rate f_{sample} compared to switching frequency f_{sw}. Apart from hysteresis and conventional PI controllers, hybrid, deadbeat predictive control laws along with nonlinear control methods, such as back-stepping and sliding mode controllers, have demonstrated [14], [15], [16], [17] accurate reference current tracking. However, these methods require extensive computation and memory in a digital controller.

Therefore, this article proposes a digital current control scheme, which combines the advantages of PI based and HC. The major objectives are, first, to have equal f_{sw} and f_{sample}, and, second to eliminate the need for LUTs. The proposed current control scheme uses the precept of digital peak current program mode control (PCPM) law, which is widely used for dc–dc converters [19]. To realize the PCPM control scheme, it is essential to maintain the continuity in sampled current. Therefore, a transformation is proposed which maps the phase-currents into an uninterrupted current signal. Also, variation of back-emf and L are incorporated in the control scheme through real-time estimations.

Manuscript received 31 May 2022; revised 27 October 2022; accepted 13 December 2022. Date of publication 27 December 2022; date of current version 14 February 2023. Recommended for publication by Associate Editor M. Su. *(Corresponding author: Rajdeep Banerjee.)*

The authors are with the Department of Electrical Engineering, Indian Institute of Technology Kanpur, Kanpur, Uttar Pradesh 208016, India (e-mail: brajdeep@iitk.ac.in; sensarma@iitk.ac.in).

Color versions of one or more figures in this article are available at https://doi.org/10.1109/TPEL.2022.3232539.

Digital Object Identifier 10.1109/TPEL.2022.3232539

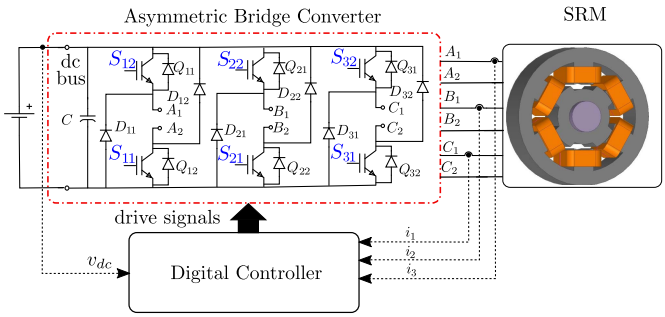

Fig. 1. Schematic diagram of the drive with a 6/4 SRM and ABC.

The rest of this article is organized as follows. Section II illustrates the mathematical modeling of SRM drives and defines the proposed transformation, leading to the dc equivalent circuit. Section III presents the derivation of the proposed parameter adaptive control law, along with the estimation of machine parameters and a robustness analysis to investigate the effect of estimation errors. Section IV presents the experimental validation on a 6/4 SRM-based laboratory prototype. Experimental results are presented and discussed for both steady state and transient operating conditions of the SRM drive. Finally, Section V concludes this article.

II. System Description and Modeling

Fig. 1 shows a schematic of an SRM drive, where an asymmetric bridge converter (ABC) is used as a power amplifier.

A. SRM

Considering that each phase is excited without overlap, mutual coupling among the phases is negligible. Therefore, the flux-linkage ψ_n corresponding to each phase is expressed as

$$\psi_n = L(i_n, \theta_n) i_n \tag{1}$$

where i_n denotes the instantaneous phase current and the phase inductance, $L(i_n, \theta_n)$ is a function of rotor position θ_n and i_n. Here, θ_n is defined with respect to the unaligned rotor position of the nth phase. Therefore, the voltage balance equation for the nth phase is expressed as

$$v_n = R i_n + \frac{d}{dt}\psi_n \tag{2}$$

$$= R i_n + L(i_n, \theta_n)\frac{di_n}{dt} + \omega i_n \frac{\partial L(i_n, \theta_n)}{\partial \theta_n} \tag{3}$$

where v_n depicts instantaneous phase voltage and R denotes the phase-resistance, assumed identical for all phases. From (3), an instantaneous back emf e_n, developed in each phase is expressed as

$$e_n = \omega i_n \frac{\partial}{\partial \theta_n}\left\{L(i_n, \theta_n)\right\}. \tag{4}$$

The reluctance torque T_n contributed by the nth phase is expressed as

$$T_n = \frac{1}{2} i_n^2 \frac{\partial}{\partial \theta_n}\left\{L(i_n, \theta_n)\right\}. \tag{5}$$

TABLE I
Different Operating Modes of ABC

Modes	S_{n1}	S_{n2}	Switches				v_n
			Q_{n1}	Q_{n2}	D_{n1}	D_{n2}	
M_1	H	H	1	1	0	0	V_{dc}
M_2	L	L	0	0	1	1	$-V_{dc}$
M_3	H	L	1	0	0	1	0
"H" $\rightarrow$high, "L" $\rightarrow$low, "1" $\rightarrow$ turned-on, "0" $\rightarrow$ turned-OFF							

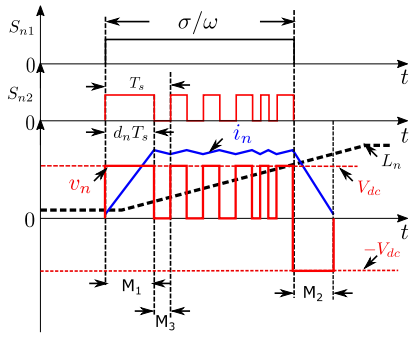

Fig. 2. Typical current waveform while it is controlled using M_1 and M_3.

Therefore, the torque balance equation is expressed as follows:

$$T_e = \sum_n T_n = J\frac{d\omega}{dt} + B\omega + T_l \tag{6}$$

where J and B are the moment of inertia and viscous coefficient, respectively. T_l and T_e denote the load and shaft torques, respectively.

B. Asymmetric Bridge Converter

Fig. 1 shows the circuit diagram of ABC for a 6/4 SRM. In this converter, each limb is dedicated to a specific phase-winding and comprises two switches $\{Q_{n1}, Q_{n2}\}$, and two diodes $\{D_{n1}, D_{n2}\}$, as shown in the figure. Based on the switching signals, it has three operating modes such as energizing (M_1), de-energizing (M_2), and freewheeling (M_3). For each mode, v_n in terms of V_{dc} is listed in Table I. Therefore, i_n can be controlled using combinations of two the operating modes, such as $\{M_1, M_3\}$ or $\{M_1, M_2\}$, for motoring operation. The former one is considered here as it causes lesser current ripple, and typical waveforms of the relevant variables are shown in Fig. 2. For motoring operation, each phase is excited in the positive gradient region of its corresponding L profile. Therefore, the switching signal S_{n1} for Q_{n2} is expressed in terms of θ_n as follows:

$$S_{n1} = \begin{cases} 1 & \theta_{on} < \theta_n < \theta_{on} + \sigma \\ 0 & \text{otherwise} \end{cases} \tag{7}$$

where θ_{on} depicts the turn-ON angle [18] and σ is the stroke angle, expressed in terms of rotor and stator pole numbers, N_r and N_s, such as

$$\sigma = 2\pi\left(\frac{1}{N_r} - \frac{1}{N_s}\right), \quad N_s > N_r. \tag{8}$$

Hence, the switching signal S_{n2}, for Q_{n1} is generated to control i_n while the respective $S_{n1} = 1$. In this mode, therefore,

v_n is expressed as

$$v_n = d_n V_{dc} \tag{9}$$

where d_n denotes the duty ratio for the nth phase. So, the duration of M_1 is $d_n T_s$, T_s being the switching period.

C. Proposed Transformation

A transformation is proposed to form an equivalent circuit model for SRM drives. As the basis of this transformation is the excitation of phases, the transformation matrix $\mathbf{P}_n$ (n-dimensional row matrix) for an n-phase SRM is expressed as

$$\mathbf{P}_n = [S_{11} \quad S_{21} \quad \dots \quad S_{n1}] \tag{11}$$

its elements being the switching signals, defined in (7). Also, since overlap in phase excitation is not considered

$$S_{11} + S_{21} + \cdots + S_{n1} = 1 \tag{12}$$

and, therefore, the following condition:

$$\mathbf{P}_n.\mathbf{P}_n^T = 1 \tag{13}$$

always holds true. Since the elements of $\mathbf{P}_n$ are binary, the pseudoinverse of $\mathbf{P}_n$ is equal to its transpose $\mathbf{P}_n^T$. Also, the time derivatives of $\mathbf{P}_n$ and $\mathbf{P}_n^T$ are

$$\frac{d}{dt}\mathbf{P}_n = [0 \quad 0 \quad \dots \quad 0], \ \frac{d}{dt}\mathbf{P}_n^T = [0 \quad 0 \quad \dots \quad 0]^T. \tag{14}$$

Therefore, a vector $\mathbf{X}$ representing an arbitrary system variable, e.g., current i_n, or the back emf e_n, in each phase of an n-phase SRM, such as

$$\mathbf{X} = [x_1 \quad x_2 \quad \dots \quad x_n]^T \tag{15}$$

is mapped into a scalar x_u by the transform $\mathbf{P}_n$ as follows:

$$x_u = \mathbf{P}_n.\mathbf{X} \tag{16}$$

while the inverse mapping uses the pseudoinverse $\mathbf{P}_n^T$ as

$$\mathbf{X} = \mathbf{P}_n^T x_u. \tag{17}$$

For any n-phase singly excited SRM, the composite voltage balance equations, as per (3) and (9), for all the n phases are expressed in (10) shown at the bottom of this page. Here, the duty-ratio d_n and current i_n corresponding to each phase are the elements of vectors, $\mathbf{D}$ and $\mathbf{I}$, respectively. Parameters $L(i_n, \theta_n)$ and its position gradient are the diagonal elements of $n \times n$ square matrices, $\mathbf{L}$ and $\mathbf{G}$, respectively. As defined in (4), the back-emf e_n corresponding to each phase is an element of the vector $\mathbf{E}$ such that

$$\mathbf{E} = [e_1 \quad e_2 \quad \dots \quad e_n]^T = \omega.\mathbf{G}.\mathbf{I} \tag{18}$$

and, using the above matrices, (10) is succinctly expressed as

$$\mathbf{D}V_{dc} = R\mathbf{I} + \mathbf{L}\frac{d}{dt}\mathbf{I} + \mathbf{E}. \tag{19}$$

Also, the developed torque T_e as per (6), is expressed as

$$T_e = \frac{1}{2}\mathbf{I}^T.\mathbf{G}.\mathbf{I}. \tag{20}$$

Therefore, the vectors of (19) are mapped into their scalar equivalents by the transform $\mathbf{P}_n$, such as

$$d = \mathbf{P}_n.\mathbf{D}, \quad i_u = \mathbf{P}_n.\mathbf{I}, \quad e_u = \mathbf{P}_n.\mathbf{E}. \tag{21}$$

Using the second relationship of (14), (19) is expressed as

$$dV_{dc} = Ri_u + \mathbf{P}_n\mathbf{L}\mathbf{P}_n^T\frac{d}{dt}i_u + e_u \tag{22}$$

where, from (18),

$$e_u = \omega\mathbf{P}_n\mathbf{G}\mathbf{P}_n^T i_u. \tag{23}$$

Hence, after the proposed transformation, the parameter matrices, $\mathbf{L}$ and $\mathbf{G}$, are mapped into dc-equivalent coefficients, L_u and α, respectively, where

$$L_u = \mathbf{P}_n\mathbf{L}\mathbf{P}_n^T = \sum_n S_{n1}^2 L(i_n, \theta_n) \tag{24}$$

$$\alpha = \mathbf{P}_n\mathbf{G}\mathbf{P}_n^T = \sum_n S_{n1}^2 \frac{\partial}{\partial\theta_n}L(i_n, \theta_n). \tag{25}$$

After the transformation, the final voltage balance equation for the equivalent circuit model is

$$dV_{dc} = Ri_u + L_u\frac{di_u}{dt} + e_u \tag{26}$$

and the developed torque is expressed as

$$T_e = \frac{1}{2}i_u^2\alpha. \tag{27}$$

This transformation superposes all the phases during their excited state to form a dc equivalent circuit with parameters R and L_u, and a current dependent back-emf component e_u ($= i_u\alpha\omega$). Similarly, the converter phases get transformed into a buck-mode switching configuration as the switch S_{n1} is always turned ON as per (12). The switching signals S_{n2} are represented as a vector $\mathbf{S}$, where

$$\mathbf{S} = [S_{12} \quad S_{22} \quad \dots \quad S_{n2}]^T. \tag{28}$$

Therefore, the switching function for the equivalent buck converter $S(t)$ is obtained after transforming $\mathbf{S}$, such that

$$S(t) = \mathbf{P}_n.\mathbf{S} = \sum_n S_{n1}S_{n2}. \tag{29}$$

$$\underbrace{\begin{bmatrix} d_1 \\ d_2 \\ \vdots \\ d_n \end{bmatrix}}_{\mathbf{D}} V_{dc} = R\underbrace{\begin{bmatrix} i_1 \\ i_2 \\ \vdots \\ i_n \end{bmatrix}}_{\mathbf{I}} + \underbrace{\begin{bmatrix} L(i_1,\theta_1) & 0 & \dots & 0 \\ 0 & L(i_2,\theta_2) & \dots & 0 \\ \vdots & \vdots & \dots & \vdots \\ 0 & 0 & \dots & L(i_n,\theta_n) \end{bmatrix}}_{\mathbf{L}} \frac{d}{dt}\begin{bmatrix} i_1 \\ i_2 \\ \vdots \\ i_n \end{bmatrix} + \omega\underbrace{\begin{bmatrix} \frac{\partial L(i_1,\theta_1)}{\partial\theta_1} & 0 & \dots & 0 \\ 0 & \frac{\partial L(i_2,\theta_2)}{\partial\theta_2} & \dots & 0 \\ \vdots & \vdots & \vdots & \vdots \\ 0 & 0 & \dots & \frac{\partial L(i_n,\theta_n)}{\partial\theta_n} \end{bmatrix}}_{\mathbf{G}}\begin{bmatrix} i_1 \\ i_2 \\ \vdots \\ i_n \end{bmatrix} \tag{10}$$

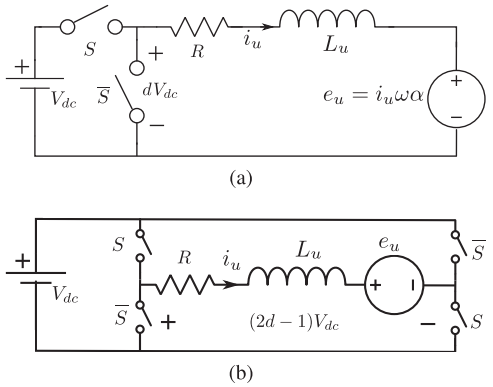

Fig. 3. Equivalent dc circuit model after the proposed transformation for current control using (a) $\{M_1, M_3\}$ and (b)$\{M_1, M_2\}$.

Obviously, the dc component of S, over a switching period T_s is

$$\langle S \rangle_{T_s} = d. \tag{30}$$

Therefore, after the transformation, Fig. 3(a) shows the equivalent model of the n-phase SRM, along with the drive converter while current is controlled using $\{M_1, M_3\}$. Similarly, the equivalent circuit is derived for the $\{M_1, M_2\}$ mode and shown in Fig. 3(b). In this scheme, driving signals for both upper and lower switches are the same element of matrix **S** and corresponding v_n is expressed as

$$v_n = (2d_n - 1)V_{dc}. \tag{31}$$

This article concentrates on the current control scheme using $\{M_1, M_3\}$ as it offers lower current ripple. Therefore, the transformed state equations, for the current control using $\{M_1, M_3\}$, are expressed as

$$\begin{aligned} \frac{di_u}{dt} &= \left(dV_{dc} - Ri_u - \omega i_u \alpha\right)/L_u \\ \frac{d\omega}{dt} &= \left(\frac{1}{2}i_u^2\alpha - B\omega - T_l\right)\Big/J \end{aligned} \tag{32}$$

where i_u and ω are the system states and d is the control input. T_l and V_{dc} depict the load and input disturbances, respectively. Since (32) is nonlinear, the small-signal linear model is derived around an arbitrary equilibrium point $\{I^e, \omega^e\}$. However, the system parameters, L_u and α, both vary with i_u and the rotor position. For the state-space model, L_u is considered as a time-varying parameter corresponding to the equilibrium point, whereas the mean, $\bar{\alpha}$ of α over the excitation region is considered. Hence, denoting the small signal perturbations, $\tilde{i}_u$, $\tilde{\omega}$, $\tilde{T}_l$ and $\tilde{d}$ in i_u, ω, T_l, and d, respectively, the linearized system model is expressed as

$$\begin{aligned} \frac{d}{dt}\begin{bmatrix}\tilde{i}_u \\ \tilde{\omega}\end{bmatrix} &= \begin{bmatrix}\frac{-(R+\omega^e\bar{\alpha})}{L_u} & \frac{-I^e\bar{\alpha}}{L_u} \\ \frac{I^e\bar{\alpha}}{J} & \frac{-B}{J}\end{bmatrix}\begin{bmatrix}\tilde{i}_u \\ \tilde{\omega}\end{bmatrix} + \begin{bmatrix}\frac{V_{dc}}{L} \\ 0\end{bmatrix}\tilde{d}_u + \begin{bmatrix}0 \\ -\frac{1}{J}\end{bmatrix}\tilde{T}_l \\ Y &= \begin{bmatrix}0 & 1\end{bmatrix}\begin{bmatrix}\tilde{i}_u \\ \tilde{\omega}\end{bmatrix} \end{aligned} \tag{33}$$

where perturbation in V_{dc} is neglected.

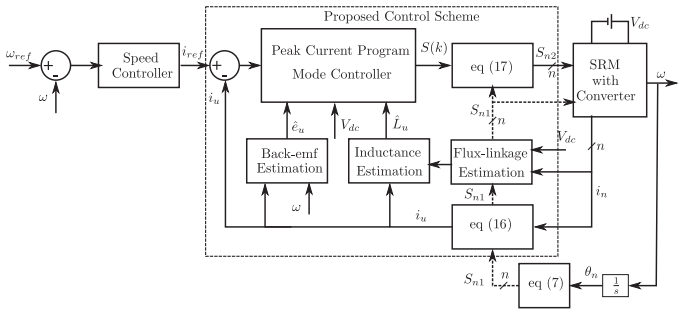

Fig. 4. Proposed current control scheme for an n-phase SRM.

From this model, the relevant transfer functions $G_c(s)$ and $G_{d\omega}(s)$ are defined and expressed as follows:

$$G_c \triangleq \frac{\tilde{i}_u(s)}{\tilde{d}(s)} = \frac{V_{dc}(s + B/J)/L_u}{s^2 + \left(\frac{R+\omega^e\bar{\alpha}}{L_u} + \frac{B}{J}\right)s + \frac{B(R+\omega^e\bar{\alpha})+(I^e\bar{\alpha})^2}{L_uJ}} \tag{34}$$

$$G_{d\omega} \triangleq \frac{\tilde{\omega}(s)}{\tilde{d}(s)} = \frac{\left(V_{dc}I^e\bar{\alpha}\right)/(L_uJ)}{s^2 + \left(\frac{R+\omega^e\bar{\alpha}}{L_u} + \frac{B}{J}\right)s + \frac{B(R+\omega^e\bar{\alpha})+(I^e\bar{\alpha})^2}{L_uJ}}. \tag{35}$$

This transformation is essential to realize the proposed parameter adaptation in the current control scheme discussed in the following section.

III. Digital Peak Current Program Mode Control Scheme

Fig. 4 shows a schematic of the proposed current control scheme for an n-phase SRM. Reference current i_{ref} is generated from the speed controller to maintain the desired speed ω_{ref}. The proposed transformation ensures continuity of current feedback i_u. This allows realization of the predictive PCPM control scheme [19], which is stable for the entire range of duty-ratios, from 0 to 1. In addition, parameters L_u and e_u are estimated online to incorporate their real-time variations. This section presents the proposed adaptive control scheme and the parameter estimation laws.

A. Adaptive Peak Current Program Mode Control Scheme

Fig. 5 shows the synthesis of the switching signal $S(t)$ generated using the following comparison:

$$S(t) = \begin{cases} 1, & V_{saw}(t) > 1 - d \\ 0, & V_{saw}(t) \le 1 - d \end{cases} \tag{36}$$

where V_{saw} is the carrier signal, its falling edge synchronized to a free-running clock with period $T_s(=1/f_{sw})$. This ensures regular sampling of peak current, at every falling edge of V_{saw}, which automatically equates the sampling frequency f_{sample} and the switching frequency f_{sw}.

Fig. 5 illustrates the operation of PCPM control scheme showing current waveform in two consecutive switching interval. The peak current $i_u[k]$ is sampled at the beginning of an arbitrary kth switching interval. In the figure, the blue solid line denotes the

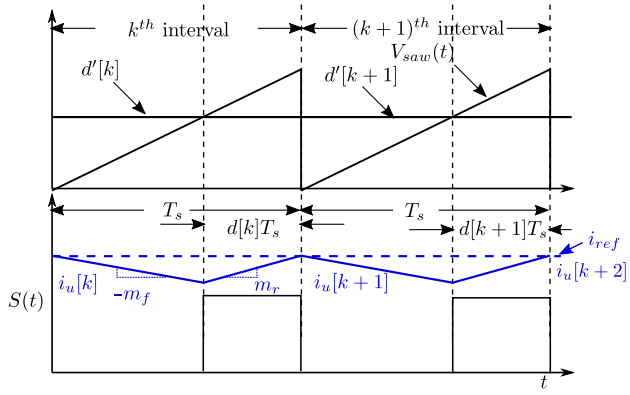

Fig. 5. Pulsewidth modulation technique along with typical current waveform, denoted by blue-line, for consecutive switching intervals at steady-state.

waveform of i_u at steady state, where m_r and $-m_f$ denote the rising and falling slopes of i_u. The relation between $i_u[k]$ and $i_u[k+1]$ is expressed as follows:

$$i_u[k+1] = i_u[k] - m_f d'[k]T_s + m_r d[k]T_s \tag{37}$$

where $d' = (1-d)$.

From (37), the duty ratio $d[k+1]$ is predicted for the $(k+1)$th switching interval from the sampled current $i_u[k]$ as follows:

$$d[k+1] = \frac{(i_{ref}[k] - i_u[k])}{(m_f + m_r)T_s} + 2\frac{m_f}{(m_f + m_r)} - d[k]. \tag{38}$$

So, pursuant to a small step in i_{ref}, at an arbitrary kth instant, error in the peak of i_u is expected to settle at the end of $(k+1)$th switching interval, or at the $(k+2)$th instant.

Now, for an SRM drive, neglecting the voltage drop across R in Fig. 3, m_r and m_f are expressed as

$$m_r = \frac{V_{dc} - e_u}{L_u}, \quad m_f = \frac{e_u}{L_u}. \tag{39}$$

Substituting (39) in (38), $d[k+1]$ is expressed as follows:

$$d[k+1] = \frac{L_u}{V_{dc}T_s}(i_{ref}[k] - i_u[k]) + 2\frac{e_u}{V_{dc}} - d[k] \tag{40}$$

where V_{dc} is sensed at each switching interval. Online estimation of L_u and e_u is carried out as follows.

B. Estimation of L_u and e_u

For the estimation laws, an assumption is made that variations in system variables and parameters within a sampling interval are negligible. Essentially using (2) for estimation, an accurate estimate $\hat{\psi}_n$ of the flux-linkage ψ_n would require the switch voltage drops to be considered along with V_{dc} to determine v_n. Therefore, governing equations for ψ_n in both switching subinterval are as follows:

$$\frac{d\psi_n}{dt} = \begin{cases} V_{dc} - (R+2R_Q)i_n - 2V_{QT} & \text{for } dT_s(M1) \\ -(R+R_Q+R_D)i_n - V_{QT} - V_{DT} & \text{for } d'T_s(M3) \end{cases} \tag{41}$$

where V_{QT} and V_{DT} denote the cut-in voltage of IGBT and diode, respectively, whereas respective ON-state resistance is denoted by R_Q and R_D. Therefore, the total switch voltage drop V_{sw} at an arbitrary kth instant, is computed using

$$V_{sw}[k] = (1+d[k])V_{QT} + d'[k]V_{DT} + ((1+d[k])R_Q + d'[k]R_D)i_n[k] \tag{42}$$

where V_{QT}, V_{DT}, R_Q, and R_D are data-sheet values. Therefore, $\hat{\psi}_n[k+1]$ is computed at each sampling instant as

$$\hat{\psi}_n[k+1] = S_{n1}\left\{(d[k]V_{dc}[k] - Ri_n[k] - V_{sw}[k])T_s + \hat{\psi}_n[k]\right\} \tag{43}$$

where R is obtained from offline measurement. However, as R varies with temperature and frequency, sensitivity of $\hat{\psi}_n$ to this variation is derived, neglecting the effect of V_{sw}, from (43), such that

$$\frac{\partial\hat{\psi}_n[k+1]/\hat{\psi}_n[k+1]}{\partial R/R} = -\left\{\frac{L/R}{T_s} + \left(\frac{d[k]V_{dc}}{Ri[k]} - 1\right)\right\}^{-1} \tag{44}$$

where $\hat{\psi}[k]/i[k]$ is equal to the phase inductance L. Since the time constant L/R is much greater than T_s and $d[k]V_{dc}$ is always greater than the resistance drop $Ri[k]$

$$\left|\frac{\partial\hat{\psi}_n[k+1]/\hat{\psi}_n[k+1]}{\partial R/R}\right| \ll 1. \tag{45}$$

Therefore, it is clear that an error in $\hat{\psi}_n$ due to the variation in R is negligible. Similarly, a small perturbation in $i[k]$ has a negligible effect on this estimation.

After computing $\hat{\psi}_n$, an uninterrupted flux-linkage signal $\hat{\psi}_u$ is obtained as follows:

$$\hat{\psi}_u = \sum_n \hat{\psi}_n \tag{46}$$

and then the estimate $\hat{L}_u$ of L_u is obtained as

$$\hat{L}_u[k] = \frac{\hat{\psi}_u[k]}{i_u[k]}. \tag{47}$$

As per (4), the back-emf depends on α, which varies with i_u and rotor position θ. From the unaligned to aligned rotor position, $L(i_n, \theta_n)$ varies monotonically with rotor position, while stator and rotor teeth are partially overlapped.

From the flux-linkage characteristics $\psi(i,\theta)$, obtained from either ofline measurements or analytical methods, the inductance profile $L(i,\theta)$ for an arbitrary rotor position θ_1, is calculated using

$$L(i,\theta_1) = \left.\frac{\psi(i,\theta)}{i}\right|_{\theta=\theta_1}. \tag{48}$$

For the SRM considered here, L_{al} and L_{un} are computed using (48), for different phase current magnitudes, from the $\psi(i,\theta)$ characteristics of machine core at the aligned position. It is observed that after a critical current, I_{sat}, L_{al} is decreasing monotonically. Fig. 6(b) shows the variation of L with θ for $i = 30$ A ($<I_{sat}$) and 70 A ($<I_{sat}$), respectively. The first-order approximations of these two L versus θ profiles are denoted by the dotted lines where the respective standard deviations are 2% and 4%, with respect to their mid-point values. Slope of each

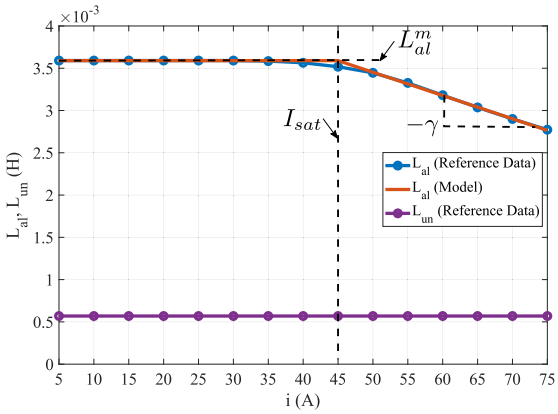

(a)

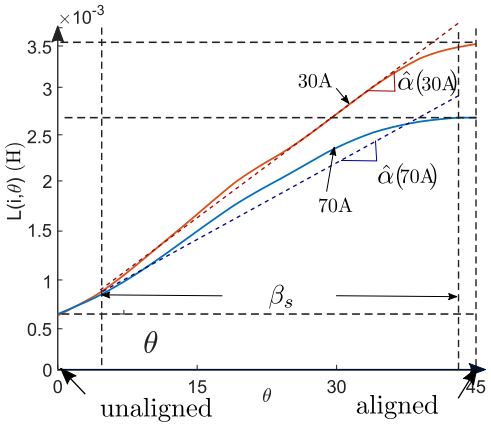

(b)

Fig. 6. (a) L_{al} and L_{un} calculated from the flux-linkage characteristics and analytical model of L_{al} as a function of excitation current, (b) L versus θ profile for different i.

dotted line denotes the corresponding $\bar{\alpha}$ which is a function of i_u due to saturation. For the linear approximated least square fit L versus θ profiles, an estimate, $\hat{\alpha}$ of $\bar{\alpha}$, for an arbitrary i_u, is computed using

$$\hat{\alpha} = \frac{L_{al}(i_u) - L_{un}}{\beta_s} \tag{49}$$

where β_s is the stator tooth-pitch. Therefore, to avoid the use of LUT, L_{al} is modeled as a function of i_u and expressed as follows:

$$L_{al}(i_u) = \begin{cases} L_{al}^m & i_u < I_{sat} \\ L_{al}^m - \gamma(i_u - I_{sat}) & i_u \geq I_{sat} \end{cases} \tag{50}$$

where L_{al}^m depicts the unsaturated inductance at aligned position and $-\gamma$ is the slope with which L_{al} decreases with current, beyond the saturation threshold current I_{sat}. Fig. 6 shows a comparison of the proposed model with the reference L_{al} data. Since the maximum modeling error is found to be -2%, an estimate $\hat{e}_u$ of the back-emf is computed using (50) as follows:

$$\hat{e}_u[k] = i_u[k]\omega[k]\hat{\alpha}[k] = i_u[k]\omega[k]\{L_{al}(i_u[k]) - L_{un}\}/\beta_s. \tag{51}$$

Finally, using $\hat{L}_u$ and $\hat{e}_u$, $d[k+1]$ is computed as follows:

$$d[k+1] = \frac{\hat{L}_u[k]}{V_{dc}[k]T_s}(i_{ref}[k] - i_u[k]) + 2\frac{\hat{e}_u[k]}{V_{dc}[k]} - d[k]. \tag{52}$$

To examine the effect of estimation errors on controller performance, a robustness analysis is carried out as follows.

C. Robustness Analysis and Design Consideration

In this analysis, it is assumed that there is no deviation in V_{dc}. Also, there are no variations in L_u and e_u within a switching interval. During steady-state operation, with no estimation errors

$$i_u[k] = i_u[k+1] = i_{ref} = I \tag{53}$$

where I denotes the steady-state current. From (37) and (39), the corresponding duty-ratio D is expressed as

$$D = \frac{e_u}{V_{dc}}. \tag{54}$$

However, an error in estimation or a perturbation in i_u at an arbitrary kth sampling instant leads to a perturbation $\Delta d[k+1]$, in $d[k+1]$ over its steady-state value. Therefore, denoting the estimation errors $\{\Delta e, \Delta L\}$, in $\{e_u[k], L_u[k]\}$, respectively, and the perturbation, $\Delta i_u[k]$, in $i_u[k]$

$$\hat{e}_u[k] = e_u + \Delta e[k],\ \hat{L}_u[k] = L_u + \Delta L[k],\ i_u[k] = I + \Delta i_u[k].$$

Also, from (52), $\Delta d[k+1]$ is derived as

$$\Delta d[k+1] = \frac{\hat{L}_u[k]}{V_{dc}T_s}(-\Delta i_u[k]) + 2\frac{\Delta e[k]}{V_{dc}} - \Delta d[k]. \tag{55}$$

Since any perturbation in d invariably affects i_u, the perturbation, $\Delta i_u[k+2]$ in $i_u[k+2]$ is derived from (37) as

$$\Delta i_u[k+2] = \Delta i_u[k+1] + \frac{V_{dc}T_s}{L_u}\Delta d[k+1]. \tag{56}$$

The perturbations in d and i_u at an arbitrary kth instant lead to a deviation in the estimated variables from their actual values. From (43), (47), and (51), the perturbations $\Delta\psi[k+1]$, $\Delta L[k]$, and $\Delta e[k]$, in $\hat{\psi}_n[k+1]$, $\hat{L}_u[k]$ and $\hat{e}[k]$, respectively, are expressed as

$$\begin{aligned} \Delta\psi[k+1] &= V_{dc}\Delta d[k]T_s + \Delta\psi[k] \\ \Delta L[k] &= \hat{L}_u - L_u = \frac{\psi + \Delta\psi[k]}{I + \Delta i_u[k]} - L_u \\ \Delta e[k] &= \omega I\Delta\alpha[k] + \omega\alpha\Delta i_u[k] \end{aligned} \tag{57}$$

where ψ denotes the actual flux-linkage. Considering the proposed model of $L_{al}(i_u)$ as per (50), an error, $\Delta e[k]$, in $e_u[k]$ due to the perturbation in $i_u[k]$ is derived from (51) as

$$\Delta e[k] = \begin{cases} \omega\alpha\Delta i_u & I < I_{sat} \\ \omega\left(\alpha - \frac{\gamma I}{\beta_s}\right)\Delta i_u & I \geq I_{sat}. \end{cases} \tag{58}$$

It is observed that an effect on e_u due to the perturbation in i_u is less while operating under magnetic saturation, compared to unsaturated condition.

TABLE II
PROPAGATION OF PERTURBATIONS IN $i[k]$, $d[k]$ AND ESTIMATED VARIABLES

k	$\frac{\Delta i_u[k]}{\Delta\alpha}$	$\frac{\Delta d[k]}{\Delta\alpha}$	$\Delta\alpha[k]$	$\frac{\Delta e[k]}{\Delta\alpha}$	$\frac{\Delta\psi[k]}{\Delta\alpha}$	$\Delta L[k]$
0	0	0	$\Delta\alpha$	ωI	0	0
1	0	$2\frac{\omega I}{V_{dc}}$	0	0	0	0
2	$2\frac{\omega I T_s}{L_u}$	$-2\frac{\omega I}{V_{dc}}$	0	$2\frac{\omega^2 I\alpha T_s}{L_u}$	$2\omega I T_s$	0
3	0	$4\frac{\omega^2 I\alpha T_s}{V_{dc}L_u}$	0	0	0	0
4	$4\frac{\omega^2 I\alpha T_s}{L_u^2}$		...	...	...	...

Now, to examine the propagation of perturbations in i_u, d and estimated variables, a small perturbation, $\Delta\alpha$, in $\hat{\alpha}$, defined as

$$\hat{\alpha}[k] = \alpha + \Delta\alpha \tag{59}$$

is introduced at an arbitrary sampling instant while the drive is operating at steady state without any estimation errors. Denoting this sampling instant as $k = 0$, the perturbations in d, i_u and the estimated variables, over subsequent sampling instants, are listed in Table II. In this analysis, it is considered that the steady-state operating current is less than I_{sat} as the effect of perturbation on $\hat{e}_u$ is significant while $I < I_{sat}$ as per (58). Therefore, there is no variation in $\hat{\alpha}$ due to the perturbed i_u. Also, though the table shows an error in $\hat{\psi}_u$ due to the perturbation in d, there is no effect on $\hat{L}_u$ due to the perturbations in both i_u and d.

For stable operation, the propagation of perturbations in i_u must be decaying. Table II shows that the perturbations in i_u appear in every alternative sampling instants, for $k > 0$. The ratio of $\Delta i_u[4]$ to $\Delta i_u[2]$ is expressed as

$$\frac{\Delta i[4]}{\Delta i[2]} = 2\frac{\omega\alpha T_s}{L_u} \tag{60}$$

where $\alpha = \hat{\alpha}$ since $\Delta\alpha$ remains 0 for $I < I_{sat}$ and $k > 0$. Therefore, substituting α as per (49) and (50), this ratio is expressed as

$$\frac{\Delta i[4]}{\Delta i[2]} = 2\frac{\omega(L_{al}^m - L_{un})T_s}{L_u\beta_s}. \tag{61}$$

Expressing ω in terms of the stroke-frequency f_{stroke}

$$\omega = \frac{2\pi}{N_r} f_{stroke} \tag{62}$$

N_r being the number of rotor poles, and substituting (62) in (61), the condition for stable operation is derived as

$$\left(\frac{4\pi}{N_r\beta_s}\right)\left(\frac{f_{stroke}}{f_{sample}}\right)\left(\frac{L_{al}^m - L_{un}}{L_u}\right) < 1. \tag{63}$$

Here $f_{sample} = 1/T_s$. Considering the worst case scenario, i.e., $L_u = L_{un}$, for stable operation, f_{sample} must follow:

$$f_{sample} > \left(\frac{4\pi}{N_r\beta_s}\right)(\lambda - 1)\, f_{stroke} \tag{64}$$

where λ denotes the saliency L_{al}^m/L_{un} in absence of magnetic saturation.

To validate the proposed scheme, experimental results with a 6/4 SRM are presented in the following section.

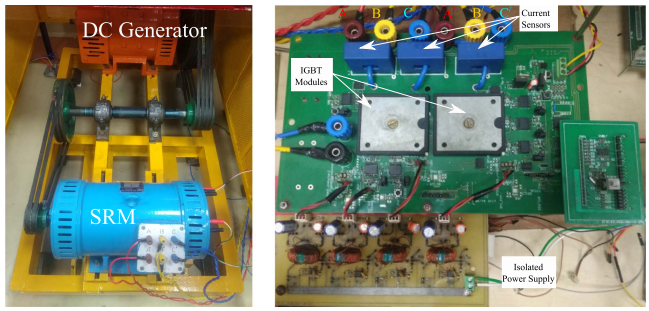

(a) (b)

Fig. 7. Laboratory prototype of a 6/4 SRM drives. (a) SRM with DC generator. (b) ABC with Auxiliary circuits.

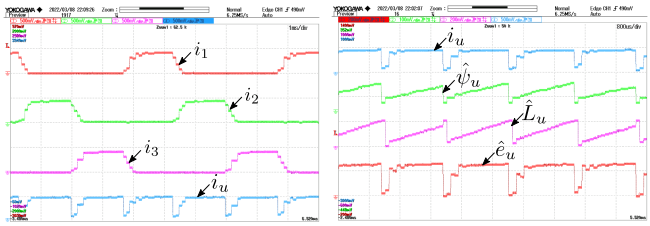

(a) (b)

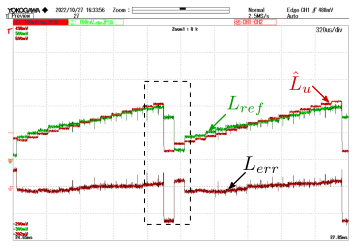

(c)

Fig. 8. Experimental results: (a) i_n $(n \in 1, 2, 3)$ mapped into i_u, and (b) estimated variables, $\hat{\psi}_u$, $\hat{L}_u$, and $\hat{e}_u$ at 3000 r/min and no-load condition, (c) errors in $\hat{L}_u$ estimation. Scale: (a) i_n $(n \in 1, 2, 3)$ and i_u (8 A/div), time: 1 ms/div; (b) i_u (8 A/div), $\hat{\psi}_u$ (30 mVs), $\hat{L}_u$: (3 mH/div), $\hat{e}_u$: (10 V/div), (c) $\hat{L}_u$, L_{ref}, L_{err}: (1.5 mH/div), time:320 μs/div.

TABLE III
DETAILS OF 6/4 SRM

Rated Power	1 kW
DC-link voltage	190 V
Maximum phase current	40 A
Rated speed	3000 r/min
Maximum developed torque	3.2 N m
Moment of inertia	0.01 Nms^2/rad
Viscous coefficient	0.0036 Nms/rad
Winding resistance/phase	0.04 Ω
Saliency (unsaturated)	6.2

IV. EXPERIMENTAL VALIDATION AND DISCUSSIONS

A. Experimental Setup and Implementation of Control Scheme

Fig. 7 shows the 6/4 SRM-based laboratory prototype. Fig. 7(a) shows the SRM coupled with a dc separately excited generator, used as a mechanical load. Machine ratings and parameters are listed in Table III.

Fig. 7 shows the laboratory fabricated ABC along with its auxiliary circuits. The proposed control law is realized on a

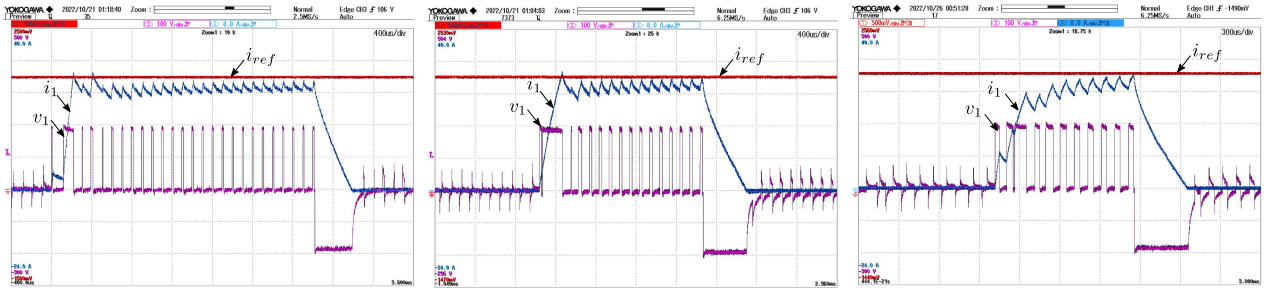

Fig. 9. Experimental results: waveforms of i_1 and v_1 while $i_{ref} = 28$ A for (a) 2000 r/min, (b) 3000 r/min, and (c) 4500 r/min. Scale: (a), (b), (c) i_1 and i_{ref} (8 A/div), v_1 (100 V/div); time: (a), (b) 400 μs/div (c) 300 μs/div.

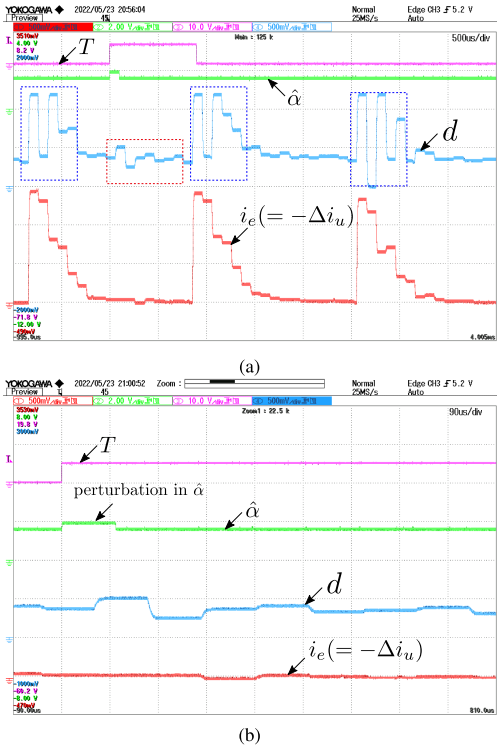

Fig. 10. Experimental result: (a) propagation of perturbations in $i_e[k]$ and $d[k+1]$ due to perturbations in $\hat{\alpha}$ and i_u, (b) zoomed view of red box in (a). Scale: (a), (b) d(0.4/div), i_e(8 A/div), $\hat{\alpha}$(1.2 mH/rad), time: (a) 500 μs/div; (b) 90 μs/div.

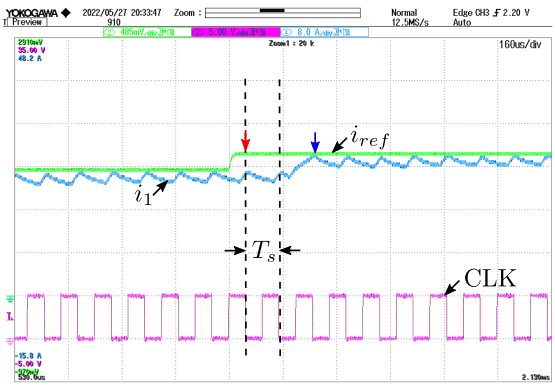

Fig. 11. Experimental result: transient response of i_1 due to a small step change in i_{ref}. Scale: i_1 and i_{ref} (8 A/div), time: 160 μs/div.

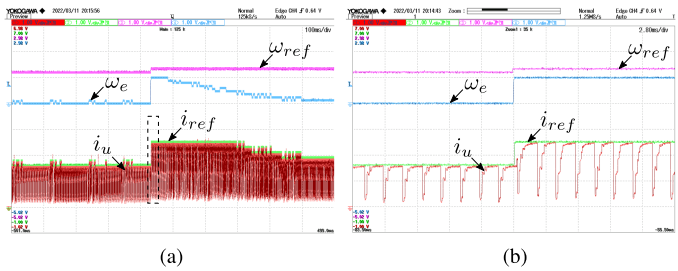

Fig. 12. Experimental result: transient response of ω_e, i_{ref} and i_u for sudden step change in (a) ω_{ref} from 3000 to 3300 r/min, (b) zoomed view. Scale: (a), (b) ω_{ref} (2400 r/min/div), ω_e (300 r/min/div), i_{ref} and i_u (16 A/div); time: (a) 100 ms/div, (b) 2.8 ms/div.

FPGA (Altera Cyclone EP1C12Q240C8) based digital platform, clocked at 20 MHz. Stability criterion (62), at rated operating condition, is satisfied by the choice of $f_{sample}\,(=f_{sw}) = 10$ kHz.

Fig. 8(a) shows the experimental result for the transform i_u of the individual phase currents using the proposed transformation. Also, Fig. 8(b) shows the experimental results of i_u along with the estimated variables $\hat{\psi}_u$, $\hat{L}_u$, and $\hat{e}_u$. It is observed that the continuity in i_u and all the estimated variables are achieved, which is essential for the adaptive PCPM control scheme. Also, an error analysis is carried out to check the accuracy of L_u estimation as shown in Fig. 8(c). Here, the reference inductance L_{ref} is obtained form an LUT, which stores the offline measured inductance in terms of i and θ. It is observed that the error in estimation, $L_{err}(=\hat{L}_u - L_{ref})$, is within the tolerable limit except during phase-transition, shown enclosed by the black dotted box. Mean and standard deviation of the errors are -4.88% and 7.8%, respectively, with respect to the midpoint inductance.

B. Robustness Analysis

As discussed in Section III-C, robustness of the control scheme depends on operating T_s and ω. Therefore, in Fig. 9, the experimental results of i_1, v_1 and i_{ref} are shown for different operating speeds (2000, 3000, 4500 r/min). From these experimental results, no oscillation in peak of i_1 is observed. Since sequential switching of the phases amounts to a large signal perturbation in i_u, these results indicate the stability and robustness of the proposed control scheme.

For experimental verification, a small perturbation $\hat{\alpha}$ in α is introduced at an arbitrary switching interval. Fig. 10 shows

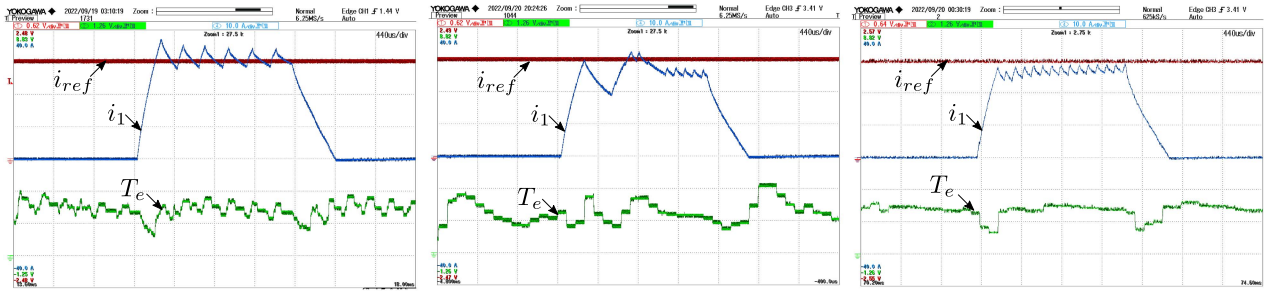

(a) (b) (c)

Fig. 13. Experimental results: waveform of i_1 and T_e while $i_{ref} = 30$ A and $\omega = 3000$ r/min, for (a) Hysteresis [13], (b) Flux-based MPC [15], and (c) Proposed PCPM current controllers. Scale: i_1 and i_{ref} (10 A/div), T_e (1 N · m/div), time: 440 μs/div.

the observed d and current error, $i_e(=i_{ref} - i_u)$, after a 20% perturbation in α is introduced at the positive edge of a marker, T. In Fig. 10(a), the blue and red boxes mark the perturbations in $d[k+1]$ due to the large-signal perturbation in i_u and small-signal perturbation in α, respectively. Fig. 10(b) shows the zoomed view of the red box of Fig. 10(a). It is observed that perturbation in $d[k+1]$ is decaying in both cases and there is an negligible effect on i_e due to perturbation in $\hat{\alpha}$. This validates the robustness of the proposed control scheme.

C. Transient Analysis

To examine the transient behavior of the proposed control scheme, a small step change 3 A, in i_{ref} is introduced in an arbitrary switching interval while $\omega = 2000$ r/min. Fig. 11 shows the experimental result of i_1 around a 3 A step in i_{ref}. Here, **CLK** denotes the digital clock signal with a period, T_s. Since i_1 is sampled at the negative edge of **CLK**, the change in i_{ref} is captured at the sampling instant marked by the red arrow. It is observed that the peak of i_1 settles at the end of the next switching interval, the instant marked by the blue arrow. Thus, it confirms the design prediction that the phase current settles in two switching intervals.

For further validation, the tracking of i_{ref} is also checked for a sudden change in ω_{ref}, which causes a large step change in i_{ref}. To limit the phase currents, upper bound of the current reference is set to 40 A. Fig. 12(a) shows the transient response of i_{ref}, i_u and ω_e for a step change in ω_{ref} from 3000 to 3300 r/min, while Fig. 12(b) is the zoomed view of the dotted box in Fig. 12(c). It is observed that i_u tracks i_{ref} excellently during steady state and transient. Also, this confirms the stability of the proposed adaptive PCPM control law.

D. Performance Comparison and Discussion

Performance of the proposed PCPM controller is benchmarked against the conventional hysteresis (HC) and the model predictive controller (MPC) [15]. The hysteresis band amplitude [13] for the HC is computed as

$$\Delta I = E(V_{dc} - E)/(2V_{dc}L_{mean}f_{sw}) \tag{65}$$

where L_{mean} is the mean phase-inductance and E the back-emf under rated conditions. ΔI is calculated for $f_{sw} = 10$ kHz to keep it equal to that of the proposed PCPM scheme, whereas f_{sample} for HC is 50 kHz. For a given reference current i_{ref}, the actual current in HC is expected to be bounded within the limits I_{upper} and I_{lower}, where

$$I_{upper} = i_{ref} + \Delta I, \quad I_{lower} = i_{ref} - \Delta I \tag{66}$$

and ΔI is decided by (65). To realize the MPC [15], 2-D look-up table is used to store the flux-linkage characteristics in terms of i and θ. Here, step size of i and θ are 0.63 A and 0.7° (mech.), respectively, and the sampling rate is 10 kHz.

Fig. 13 shows the experimental waveform of i_1 and T_e while $I_{ref} = 30$ A at 3000 r/min, for these three current control schemes. From the experimental waveform, it is clear that the proposed scheme accurately tracks the reference current, compared to the conventional methods. To quantify performance of these controllers, various metrics, such as average developed-torque (T_{avg}), peak-to-peak torque ripple (T_{pp}), torque quality ($T_{quality}$), and root-mean-square (I_{rsme}) of current error, are evaluated while $I_{ref} = 30$ A, at $\omega = 3000$ r/min. These metrics are listed in Table IV. Here, the torque quality is calculated in percentage as follows:

$$T_{quality} = \frac{T_{pp}}{T_{avg}} \times 100\%. \tag{67}$$

From the experimentally measured data, it is clear that the proposed scheme offers higher accuracy in reference tracking and minimum torque ripple compared to the conventional schemes.

TABLE IV
COMPARISON WITH EXISTING SCHEMES

	Hysteresis [13]	Flux-based MPC [15]	Proposed PCPM
I_{ref}	30 A		
T_{avg}	1.47 N m	1.26 N m	1.37 N m
T_{pp}	1.59 N m	1.47 N m	0.96 N m
$T_{quality}$	108%	116%	70%
I_{rmse}	10.75 A	14.5 A	7.48 A
η_{conv}	84.9%	85.7%	85.5%
η_{SRM}	83.9%	83.2%	83.5%

V. CONCLUSION

This article has presented a digital peak current program mode control scheme for SRM drives. A novel transformation was first proposed to map all phase-currents into an uninterrupted

current signal. A predictive current control law was used, which totally obviated complications regarding the design of controller coefficients in the conventional PI controller. From a robustness analysis to examine the impact of estimation error on duty-ratio and phase current, a stability criterion is derived which dictates the minimum limit for switching or sampling frequency, considered numerically identical here. The proposed control scheme is experimentally validated with a 6/4 SRM drive prototype. Robustness of the proposed scheme was experimentally validated at different rotor speeds by injecting perturbations in the estimated back-emf. Excellent current command following, with a 2-sample settling time, was experimentally demonstrated for a small step command. Finally, performance of the proposed scheme was experimentally benchmarked against conventional HC and MPC schemes. The experimental results clearly confirm that the proposed scheme outperforms the existing schemes in terms of torque quality and reference current tracking.

ACKNOWLEDGMENT

The authors would like to acknowledge Mr. Amit Kr. Basu, Mr. Nand Kishore, and Mr. Satyendra Kumar for their support during development of the experimental setup.

REFERENCES

[1] A. Chiba and K. Kiyota, "Review of research and development of switched reluctance motor for hybrid electrical vehicle," in *Proc. IEEE Workshop Elect. Machines Des., Control Diagnosis*, 2015, pp. 127–131.
[2] X. D. Xue et al., "Study of motoring operation of in-wheel switched reluctance motor drives for electric vehicles," in *Proc. IEEE 3rd Int. Conf. Power Electron. Syst. Appl.*, 2009, pp. 1–6.
[3] S. P. McDonald, G. J. Atkinson, R. Martin, and S. Ullah, "Magnetically biased inductor for an aerospace switched reluctance drive," *Proc. IEEE Int. Electric Mach Drives Conf.*, 2015, pp. 1272–1278.
[4] A. K. Mishra and B. Singh, "Solar photovoltaic array dependent dual output converter based water pumping using switched reluctance motor drive," *IEEE Trans. Ind. Appl.*, vol. 53, no. 6, pp. 5615–5623, Nov./Dec. 2017.
[5] H. K. Bae and R. Krishnan, "A study of current controllers and development of a novel current controller for high performance SRM drives," in *Proc. IEEE Conf. Rec. Ind. Appl. Conf.*, 1996, vol. 1, pp. 68–75.
[6] X. Wang and Jih-Sheng Lai, "Small-signal modeling and control for PWM control of switched reluctance motor drives," in *Proc. IEEE 33rd Annu. Power Electron. Specialists Conf.*, 2002, pp. 546–551, vol. 2.
[7] G. Schroder and J. Bekiesch, "Adaptive current control for the SRM," *Proc. IEEE Int. Symp. Ind. Electron.*, 2005, pp. 69–74.
[8] S. Schulz and K. Rahman, "High–performance digital PI current regulator for EV switched reluctance motor drives," *IEEE Trans. Ind. Appl.*, vol. 39, no. 4, pp. 1118–1126, Jul./Aug. 2003.
[9] H. Hannoun, M. Hilairet, and C. Marchand, "High performance current control of a switched reluctance machine based on a gain-scheduling PI controller," *Control Eng. Pract.*, vol. 19, no. 11, pp. 1377–1386, 2011.
[10] S. S. Ahmad and G. Narayanan, "Linearized modeling of switched reluctance motor for closed-loop current control," *IEEE Trans. Ind. Appl.*, vol. 52, no. 4, pp. 3146–3158, Jul./Aug. 2016.
[11] A. V. Rajarathnam, K. M. Rahman, and M. Ehsani, "Improvement of hysteresis control in switched reluctance motor drives," in *Proc. IEEE Int. Elect. Mach. Drives Conf.*, 1999, pp. 537–539.
[12] R. Banerjee, M. Sengupta, and S. Dalapati, "Design and implementation of current mode control in a switched reluctance drive," in *Proc. IEEE Int. Conf. Power Electron., Drives Energy Syst.*, 2014, pp. 1–5.
[13] H. Maamri, I. Bahri, and N. Derbel, "Adaptive hysteresis controller for the switched reluctance machines," in *Proc. IEEE Int. Conf. Elect. Sci. Technol. Maghreb*, 2014, pp. 1–6.
[14] M. W. Arab, X. Rain, M. Hilairet, P. G. Estébanez, H. Hannoun, and C. Marchand, "Design of an enhanced adaptive hybrid controller for switched reluctance motors," in *Proc. IEEE 39th Annu. Conf. Ind. Electron. Soc.*, 2013, pp. 6602–6607, doi: 10.1109/IECON.2013.6700224.
[15] R. Mikail, I. Husain, Y. Sozer, M. S. Islam,, and T. Sebastian, "A fixed switching frequency predictive current control method for switched reluctance machines," *IEEE Trans. Ind. Appl.*, vol. 50, no. 6, pp. 3717–3726, Nov./Dec. 2014, doi: 10.1109/TIA.2014.2322144.
[16] M. T. Alrifai, J. H. Chow, and D. A. Torrey, "Practical application of backstepping nonlinear current control to a switched-reluctance motor," in *Proc. Amer. Control Conf.*, 2000, vol. 1, pp. 594–599.
[17] Z. Ruiwei, Q. J. Xisen, Z. Liping, Z. Yingchao Tianwen, and N. Jintong, "An adaptive sliding mode current control for switched reluctance motor," in *Proc. IEEE Conf. Expo Transp. Electrific. Asia-Pacific*, Beijing, China, 2014, pp. 1–6.
[18] I. Kioskeridis and C. Mademlis, "A unified approach for four-quadrant optimal controlled switched reluctance machine drives with smooth transition between control operations," *IEEE Trans. Power Electron.*, vol. 24, no. 1, pp. 301–306, Jan. 2009, doi: 10.1109/TPEL.2008.2005983.
[19] J. Chen, A. Prodic, R. W. Erickson,, and D. Maksimovic, "Predictive digital current programmed control," *IEEE Trans. Power Electron.*, vol. 18, no. 1, pp. 411–419, Jan. 2003, doi: 10.1109/TPEL.2002.807140.
[20] R. Banerjee and P. Sensarma, "Improved analytical method to determine flux-linkage characteristics of a switched reluctance machine," *IEEE Trans. Ind. Appl.*, vol. 56, no. 6, pp. 6314–6323, Nov./Dec. 2020, doi: 10.1109/TIA.2020.3012105.

Rajdeep Banerjee (Student Member, IEEE) received the B.Tech. degree from Maulana Abul Kalam Azad University of Technology (erstwhile West Bengal University of Technology), Kolkata, India, in 2012, and the M.E. degree from Indian Institute of Engineering Science and Technology, Shibpur, India, in 2014, both in electrical engineering. He is currently working toward the Ph.D. degree in switched reluctance machine drives for traction applications with the Department of electrical engineering, Indian Institute of Technology, Kanpur, India.

His research interest includes electrical machine design, electromagnetic analysis, and control of machine-drives.

Parthasarathi Sensarma (Senior Member, IEEE) received the B.E.E degree from Jadavpur University, Kolkata, India, in 1990, the M.Tech degree from the Indian Institute of Technology (IIT) Kharagpur, Kharagpur, India, in 1992, and the Ph.D. degree from Indian Institute of Science Bangalore, Bangalore, India, in 2001, all in electrical engineering.

He had held positions at Bharat Bijlee Ltd., Thane, India; CESC Ltd., India; and ABB Corporate Research, Baden-Daettwil, Switzerland, where he was a Scientist in the Power Electronics Department. Since 2002, he has been with the Department of Electrical Engineering, IIT Kanpur, Kanpur, India, where he is currently a Professor. He teaches courses on power electronics and electrical engineering. His research interests include electrical machines and drives, power quality, flexible ac transmission system devices, power converters, and renewable energy integration.